Project FORTE - Nuclear Thermal Hydraulics Research & Development

Assessment of RANS Turbulence Model Performance in Tight Lattice LWR Fuel Subchannels

August 2019

FNC 53798/48654R Issue 1

SYSTEMS AND ENGINEERING TECHNOLOGY

FRAZER-NASH CONSULTANCY

An introduction to Project FORTE

The Department for Business, Energy and Industrial Strategy (BEIS) has tasked Frazer-Nash Consultancy and its partner organisations to deliver the first phase of a programme of nuclear thermal hydraulics research and development.

Phase 1 of the programme comprises two parts:

- The specification and development of innovative thermal hydraulic modelling methods and tools; and
- The specification of a new United Kingdom thermal hydraulics test facility.

The work is intended to consider all future reactor technologies including Gen III+, small modular reactors and advanced reactor technologies.

Our project partners

The team is led by Frazer-Nash Consultancy and includes:

FRAZER-NASH CONSULTANCY

The University Of Sheffield.

EDF ENERGY

Westinghouse

MANCHESTER 1824
The University of Manchester

Science & Technology Facilities Council

For more information, visit www.innovationfornuclear.co.uk/nuclearthermalhydraulics.html

Executive Summary

The objective of this work has been the assessment of state-of-the-art RANS models in the simulation of turbulent flows through PWR fuel cooling passages. This is one of the most critical areas of thermal hydraulic importance within the reactor since the rate at which thermal energy is removed from the fuel pins determines the reactor maximum operating temperature and therefore impacts both performance and safety. The assessment has been carried out with a view to providing information and a referenceable source of evidence regarding the advantages and disadvantages of the different models. The provision of guidance and demonstration of the use of state-of-the-art modelling in a nuclear application being a key enabler to the use of these methods in an industrial context.

The research involved the use of a variety of RANS modelling practices. Some have resulted from innovative research at Manchester University (cubic non-linear k-epsilon models and analytical wall functions) and other centres of excellence (the Hanjalić and Jakirlić low-Re second-moment closure) and some are more established models widely used in industrial simulations, such as the high-Re k-ε and the k-ω SST models.

The test-case selected for comparisons with experimental data is the single-phase turbulent flow of air through a square pitched 2x3 array of cylindrical rods (Hooper 1980). The fully-developed flow operates at a Reynolds number of $Re = 48000$ and the pitch to diameter ratio of the rods is 1.194. Though the experimental study is relatively old, Hooper presented a comprehensive selection of measurements, including mean axial velocity, wall shear stresses, pressure drops and, crucially for turbulence model assessment, all six Reynolds stress tensor components.

Results show that the predictions are dependent on both the choice of turbulence model and near-wall modelling approach. The following key conclusions have been drawn from this work:

- Low-Re models demonstrated consistently better overall performance, due to their ability to reproduce the correct near-wall behaviour, with the full stress transport closure of Hanjalić & Jakirlić (HJ) providing the best quantitative agreement. They are recommended over high-Re approaches if computational resources allow.
- Whilst the superiority of the low-Re near-wall approach is clear for the flow studied in this case, for higher Reynolds number flow, such as would be seen in a PWR under normal operation, the overall impact of not resolving the viscosity affected near-wall region (i.e. a wall function approach) may be reduced, since the viscous layer becomes much thinner.
- If a low-Re near-wall approach is not computationally feasible, then analytical wall functions offer noticeable improvements over standard wall functions, owing to their ability to account for near-wall convection and pressure gradient effects. In the case studied in this report, use of the standard wall functions produced predictions that differed significantly from the experimental results.
- In sub-channel flows of this type, secondary flows can produce noticeable alterations in the mean axial velocity distribution and would be likely to affect the heat transfer from the fuel. Approaches based on the linear eddy-viscosity formulation cannot capture this, owing to their inability to account for anisotropy in the Reynold stresses; ideally a stress transport approach is required.
- Models have been assessed against detailed data which was openly available and obtained from a representative yet suitably simple geometry. However, data of this type was found to be scarce. There is a clear need for more openly available, high-quality ‘CFD-grade’ experimental and numerical datasets for flows relevant to nuclear thermal hydraulics to allow further testing and assessment.

Contents

1 Introduction

Fuel assemblies in many nuclear reactors are, when stripped to their most basic geometric elements, simply collections of cylindrical fuel rods arranged in a square (PWR/BWR), hexagonal (VVER) or circular (CANDU, AGR) array. The basic thermal hydraulic function of these fuel assemblies is to facilitate the transport of thermal energy away from the fuel rods and into the primary coolant loop outside the main reactor vessel. This is achieved by pumping the coolant axially along the length of the fuel assemblies, with the spaces between the fuel rods, typically referred to as sub-channels, providing the primary flow passage geometry. Adjacent sub-channels are typically connected by a gap, the size of which is defined by the pitch-to-diameter ratio P/D of the rod assembly. Whether or not the fuel assembly is hydraulically isolated from its neighbours depends on the reactor type; PWR assemblies are not whilst BWR assemblies are.

From a purely hydraulic perspective, the fuel sub-channels can be considered simply as a series of interconnected axial flows of non-circular cross-section. Both these geometric features (i.e. interconnectedness and non-circular cross-section) have been shown to generate influential flow patterns which are not found in the more frequently studied pipe and channel geometries.

Firstly, any wall-bounded turbulent flow of non-circular cross section will display mean fluid motion in a plane perpendicular to the main axial flow, termed “secondary flow of the second kind” by Prandtl (1952), owing to the anisotropic distribution of the cross-stream normal stresses. This phenomenon, verified extensively by early experimentation (Brundrett & Baines 1964; Gessner & Jones 1965; Hoagland 1962) and later by direct numerical simulation (Huser & Biringen 1993), sets up a system of counter rotating vortices which tend to transport high momentum fluid away from the centre of the duct towards the corners (if they exist). Whilst the magnitude of these motions is typically only 1-2% of the main axial flow, they do modify the axial velocity distribution within the cross-section, and so can have considerable effects on the mixing of momentum, heat and the turbulent stresses themselves. The anisotropic nature of the Reynolds stress field which generates this secondary motion means that turbulence modelling approaches based on the linear eddy-viscosity assumption will, a priori, not be able to account for this effect.

The second feature of note relates to the interconnectedness of adjacent sub-channels. As described in a review by Meyer (2010), early experiments on rod bundles found unusually high inter-channel mixing rates which could not be adequately accounted for by turbulent diffusion alone. Many authors attributed this to the presence of Prandtl’s secondary motions discussed above, since they did produce flow patterns that would, at least qualitatively, account for the additional mixing. Later experiments (Meyer & Rehme 1994; Rehme 1987; Rowe *et al.* 1974), however, demonstrated the presence of previously unseen periodic large scale vortices which travelled axially between neighbouring sub-channels and were not associated with the secondary motion. The existence of these travelling vortices (termed a ‘vortex train’ by Meyer (2010)), has now been confirmed with high-fidelity numerical simulations by a number of authors (Biemüller *et al.* 1996; Ikeno & Kajishima 2010; Mayer & Házi 2006) but disagreement on their physical origin still exists.

From the above literature, it is clear that the novel geometries provided by nuclear fuel assemblies result in the generation of some fairly nuanced flow phenomenology. Whilst current state-of-the-art high-fidelity CFD (i.e. Large Eddy Simulation and Direct Numerical Simulation) is certainly capable of reproducing these kinds of flows (see, for example, Duan and He (2017)) the high computation power requirements currently prohibit their application in the domains of

larger size and complexity typically required for nuclear thermal hydraulics phenomena. Current numerical modelling practice within the nuclear industry favours the use of thermal hydraulic 'system codes' and 'sub-channel codes', which both use a number of limiting simplifications to provide a very coarse (even by lower-fidelity CFD standards) numerical model of an entire reactor system or a large section of the core. Whilst well validated for some nuclear specific test cases and reactor designs, the low fidelity of the results limits both the variety of phenomena that can be captured, and the depth of the analysis that can be performed.

Since CFD codes in general, and the RANS turbulence modelling approach in particular, have reached a degree of maturity, their application to flows relevant to nuclear thermal hydraulics, such as the fuel sub-channels discussed above, will clearly be of interest to the nuclear engineering community. As well as offering potential for improvements in the thermal hydraulic performance of these sub-channels, detailed explorations of these flows will also contribute towards the overall continued assessment and development of turbulence models within the RANS framework.

A key enabler for the use of such models by industry is their demonstration in context and validation of the numerical predictions by comparison with experimental data. One suitable sub-channel experiment identified for this purpose is that by Hooper (1980). This study examined the turbulent, fully developed, flow of air through a 2x3 rod bundle (i.e. two adjacent sub-channel sections) and provided detailed measurements of the mean flow and turbulent stresses at two different pitch to diameter ratios.

This report aims to provide demonstration and assessment of the current state-of-the-art in RANS turbulence modelling by reproducing the experimental results of Hooper (1980) using their exact geometric configuration. This work builds on related studies by including a wider range of more advanced turbulence models (linear eddy-viscosity, non-linear eddy-viscosity and stress transport) and different near-wall treatments (low-Re and wall functions). The intention is that the findings of this work can be used to enable selection of the best modelling approach and to provide confidence in the accuracy of the predictions.

A description of the Hooper experiments is given in Section 2; the modelling methodologies tested are described in Section 3 (with further details given in Annex A); the results are presented in Section 4; and the conclusions are summarised in Section 5.

2 Experiments of Hooper (1980)

Hooper (1980) performed an experimental study of the developed single-phase turbulent flow of air through a square pitched array of rod bundles. In the experimental rig, a centrifugal blower passed air through piping into a settling drum, where it passed through an internal fine-mesh screen before entering the 9.14m test section. The test section contains 6 circular rods arranged in a 2x3 square array, as shown by the cross-section in Figure 1, with two pitch-diameter ratios considered: $P/D = 1.107$ and 1.194. These correspond to Reynolds numbers of $Re = 48{,}400$ and $Re = 48{,}000$ respectively.

Of note in the test section is the blanking of all of the gaps between the rods except for the two central rods, creating effectively two interconnected sub-channels. Measurements provided include mean velocity distributions, obtained using Pitot probes, the wall shear stress along the top and bottom middle rods, measured using Preston tubes and the six-components of the Reynolds stress tensor, measured by hot-wire anemometry.

Although the experimental study by Hooper is relatively old, a number of more recent studies (see, for example, Conner et al. 2010; Wells et al. 2016) either did not openly provide suitably detailed data, or dealt with larger and more complex geometrical arrangements (i.e. full length 5x5 fuel bundles with spacer grids). This makes an in-depth appraisal of the various turbulence models much more difficult to achieve, since it becomes harder to attribute model deficiencies to the flow effects that cause them.

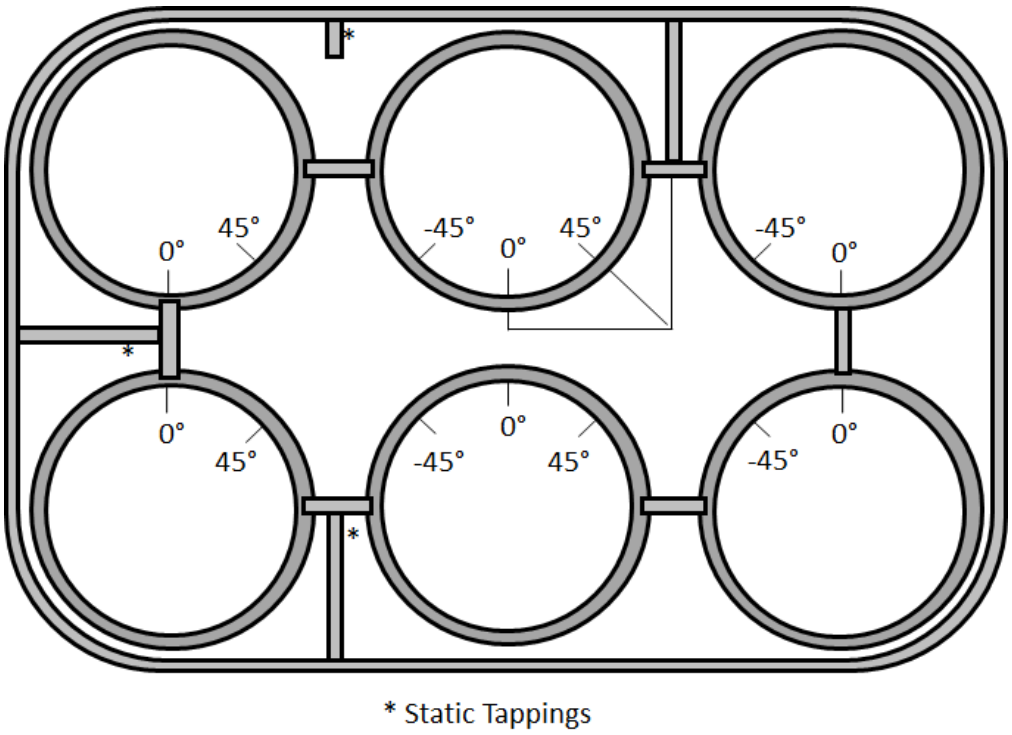

Figure 1: Cross-section of the test section used by Hooper (1980)

3 Numerical modelling

3.1 Geometry and Mesh

As discussed in Section 1, a number of previous studies have revealed the existence of periodic, 'pulsating' vortex-like structures which were seen to be a source of inter-channel mixing. Whilst Hooper did not report detecting such transient behaviour in the experiments, a number of preliminary computations have been conducted with a section of the full 3D geometry (axial length of $16D_h$) to see if a modern CFD modelling approach predicted them to be present. All 3D analyses predicted steady flow and thus a 2D representation of the cross-section with axial periodicity has been used in the primary investigation.

Preclusion of the unsteady inter-channel mixing leads to the expectation that the flow will be steady, and symmetric about the vertical centreline (of Figure 1). Although it would be possible to exploit this, the existence of axial periodicity significantly reduced mesh requirements such that the extra computational demand posed by considering both sub-channels was not of concern. This would also enable any asymmetry, if it were to be present, to be captured although, as expected, all of the results obtained were symmetric. The P/D ratio is chosen to be the larger of the two considered by Hooper $P/D = 1.194$, since this is closer to the ratio typically encountered in modern LWR fuel assemblies ($P/D = 1.38$). A schematic of the sub-channel geometry can be seen in Figure 2.

Two types of mesh were produced to reflect the needs of the two near-wall turbulence modelling approaches considered. For the wall function approach, the first node is positioned such that the non-dimensional distance from the wall $y^+ = yu_\tau/\nu \approx 30$, whilst for the low-$Re$ approach this is reduced to $y^+ \approx 1$. Both meshes use block-structured hexahedral elements with smoothing applied to improve orthogonality. To assess grid-independence, three meshes of increasing nodal density were generated for each approach. Mesh parameters can be found in Table 1 and representative images of the meshes are shown in Figure 3. All meshes were produced using the ANSYS ICEM-CFD meshing package.

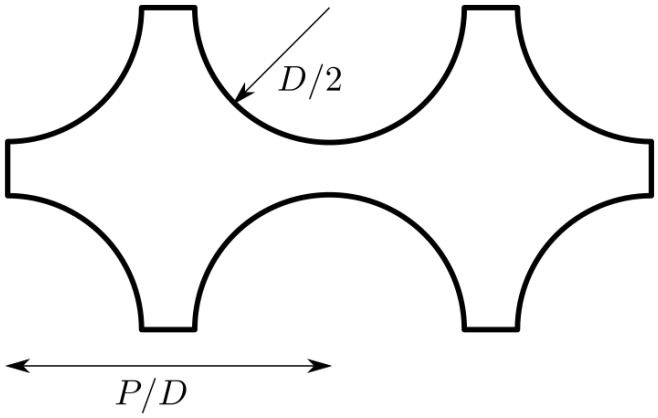

Figure 2: Case geometry

Mesh	Number of cells (N)
Wall function meshes	
swf-r1	14,500
swf-r2	36,880
swf-r3	71,538
swf-r4	227,898
Low-Re meshes	
lre-r1	45,700
lre-r2	49,680
lre-r3	104,256
lre-r4	236,800

Table 1: Mesh resolutions for mesh sensitivity tests

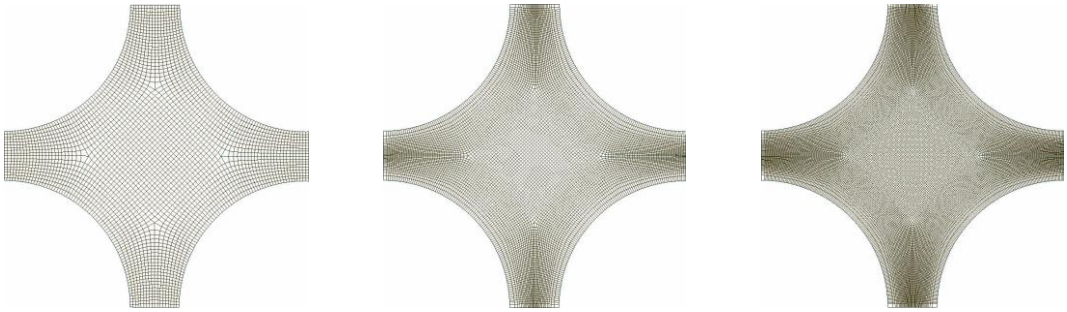

swf-r1 swf-r2 swf-r3

Wall function approach

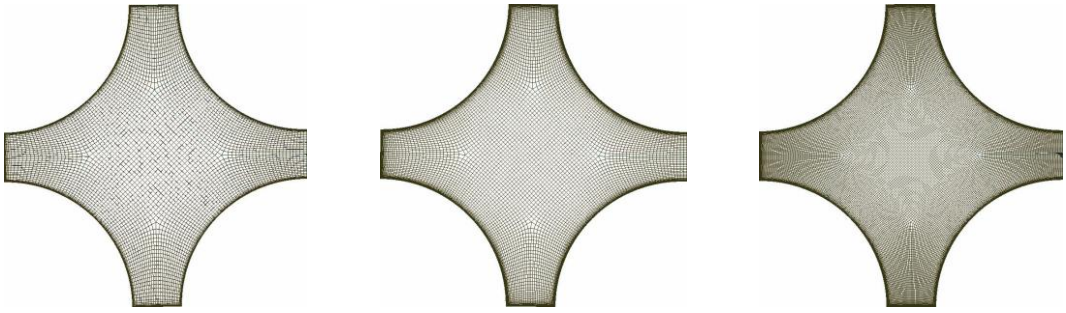

lre-r1 lre-r2 lre-r3

Low Reynolds approach

Figure 3: Selected meshes produced for both near-wall modelling approaches employed, increasing in resolution from left to right

3.2 Governing Equations

The equations governing steady-state incompressible turbulent flow comprises the continuity and Reynolds-Averaged Navier-Stokes (RANS):

$$\frac{\partial U_i}{\partial x_i} = 0 \quad (1)$$

$$U_j \frac{\partial U_i}{\partial x_j} = -\frac{1}{\rho}\frac{\partial P}{\partial x_i} + \frac{\partial}{\partial x_j}\left[\nu\left(\frac{\partial U_i}{\partial x_j} + \frac{\partial U_j}{\partial x_i}\right) - \overline{u_i u_j}\right] \quad (2)$$

where the provision of the Reynolds stresses, $\overline{u_i u_j}$, depends upon the turbulence model employed.

3.2.1 Turbulence modelling

As discussed further within the thermal hydraulic modelling critical review (Laurence *et al.* 2019), there are three main classes of turbulence model within the RANS framework:

- Linear Eddy-Viscosity Models (EVM), which suppose a linear relationship between the turbulent stresses and the mean strains through an eddy-viscosity;
- Non-linear Eddy-Viscosity Models (NLEVM), which extends that relationship to include non-linear terms: and
- Reynolds Stress Models (RSM) or stress transport models, which solve transport equations for each component of the Reynolds stress tensor, $\overline{u_i u_j}$.

To ensure this assessment is as comprehensive as possible, turbulence models have been selected to ensure representation across all three of these classes. Models are additionally split according to their approach to the near-wall region. High-Re models cannot be solved right up to the wall, and instead rely on wall functions to relate the wall-shear stress to local quantities at the near wall node. Low-Re models can be solved right up to the wall and include additional damping terms to ensure validity within the near-wall sublayer.

Table 2 details the turbulence models used in this work. Both high (HR) and low-Re (LS) forms of the 'standard' k-ε two-equation model have been tested, along with the k-ω SST model (FM) of Menter (1994), which is a hybrid model that essentially blends a k-ε type model in the far-field with a k-ω model near the wall through the use of a blending function. The Gibson & Launder (1978) RSM (GL), which adds a wall-reflection term to the 'isotropization' of production based model of Launder *et al.* (1975), and the Craft & Launder (1992) RSM (CL), which modified this wall-reflection term to more accurately account for flows with large wall-normal straining, have also been tested.

The KS model extends the k-ε model with the inclusion of cubic terms in the stress-strain relationship and has demonstrated good performance in flows affected by curvature and impingement (Craft *et al.* 1996). Finally, the low-Re RSM of Jakirlić & Hanjalić (1995) (HJ), which aims to extend the applicability of the GL RSM closure to flows with significant low-Re and wall-proximity effects, has also been tested. This has demonstrated superiority to eddy-viscosity type models over a range of non-equilibrium (Hanjalić *et al.* 1997) and swirling flows (Jakirlic *et al.* 2002). A brief, but complete, mathematical description of the models used can be found in Annex A1.

Code	Type	Reference
High-Re Wall Function		
HR	k-ε	Launder & Spalding (1974)
GL	RSM	Gibson & Launder (1978)
CL	RSM	Craft & Launder (1992)
Low-Re Approach		
LS	k-ε	Launder & Sharma (1974)
FM	k-ω SST	Menter (1994)
KS	Non-linear k-ε	Craft *et al.* (1996)
HJ	RSM	Jakirlić & Hanjalić (1995)

Table 2: Turbulence models and wall treatments used in this study

3.2.2 Near-wall modelling

The presence of a wall in a particular flow, and specifically the existence of the no-slip condition on the velocity, ensures that viscous effects will always be influential in the region just adjacent to the wall, regardless of how high the Reynolds number of the bulk flow is. To correctly account for this near-wall viscosity-affected layer, CFD computations of turbulent flow generally employ one of two strategies:

1. A numerical mesh fine enough to properly resolve the steep near-wall velocity gradients, and requires turbulence models to incorporate terms which properly account for the increased influence of viscosity. This requirement on the near-wall mesh can quickly become computationally prohibitive in even moderately high-Re flows.
2. So-called wall functions, designed to alleviate the fine mesh requirements, to provide a (generally) algebraic relationship between variables at the wall and variables at the first computational node adjacent to the wall. This requires the first node to be placed outside of the viscous sublayer, essentially removing the need to computationally resolve the viscous sublayer.

Two wall function approaches have been considered in this work. The first, generally referred to as the Standard Wall Function (SWF), is based on the well-known *law of the wall*, which uses the assumption of local equilibrium (amongst others) in the near-wall turbulence to formulate an expression for the velocity as a function of the distance from the wall. The required wall fluxes can then be computed using this expression. Despite enjoying substantive use over the past five or six decades, many of the underlying assumptions behind the approach break down in even mildly complex flows; those involving impingement, rotation, separation or buoyancy for example. Their widespread use, however, means it is relevant to continue to assess their performance, even if it only serves to continue to highlight their deficiencies.

In order to address many of the deficiencies in the standard wall function approach, but also retain its overall framework and essence, work conducted at UMIST[1] during the early 2000's led to the development of a so-called "Analytical Wall Function" (AWF) (Gerasimov 2004). The approach is based on the analytical solution of simplified near-wall momentum and temperature equations, accounting for pressure gradients, convection effects, and other force fields such as

[1] University of Manchester Institute of Science and Technology

buoyancy. It has demonstrated considerable success in a range of flows, including mixed convection flow in a vertical pipe and a two-dimensional wall jet (Craft *et al.* 2002, 2006). Full details of both the standard wall function and the analytical wall function are provided in Appendix A2.

3.3 CFD Model Solver

The computations reported as part of this work have been computed using an extended version of the STREAM code (Lien & Leschziner 1994a), which is a fully elliptic 3D finite volume solver capable of handling multi-block structured non-orthogonal meshes. It uses a collocated grid arrangement where all variables are stored at the cell centres and a Rhie and Chow interpolation scheme to obtain velocities at cell faces.

Convective terms for all transport equations have been treated with the Upstream Monotonic Interpolation for Scalar Transport (UMIST) scheme of (Lien & Leschziner 1994b), which is a bounded, monotonic implementation of the quadratic QUICK interpolation scheme. The code utilizes the standardized Message Passing Interface (MPI) for parallelisation. As a standard general 3D finite-volume solver, results obtained with the STREAM code should, in principle, be comparable to any other CFD solver which implements and solves the equations described in Section 3.2.

4 Results

4.1 Mesh sensitivity tests

Mesh sensitivity tests were conducted to ensure that the specific mesh used had minimal influence on the results. The highest resolution mesh for the wall function approach, swf-r4, was discarded on inspection, since the requirement to have the first node position fixed at $y^+ \approx 30$ meant a significant jump in cell size was present (from the first near-wall cell to the second).

Figure 4 shows the results of these tests for the low-Re meshes, with comparisons of both the normalised wall shear stress[2] ($\overline{\tau_w}$) along the top central rod wall, and the normalised velocity[3] (U^+) profile along the central rod gap, against the experimental data of Hooper. Mesh refinement had only a minor effect on the wall shear stress, but significant improvements can be seen in the velocity profiles for those meshes finer than lre-r1. Figure 5 provides a similar comparison for the high-Re meshes (those requiring a wall function approach) where, again, only minor differences can be seen. For the low-Re computations mesh revision 3 (i.e. lre-r3) was selected for further computations. For the high-Re meshes, revision 2 (swf-r2) was selected to minimise the large jump in cell size as one moves away from the wall.

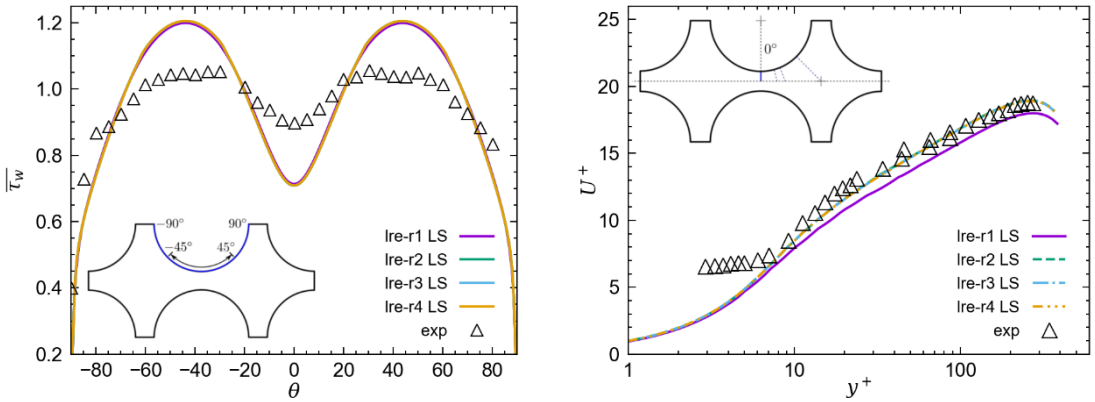

(a) (b)

Figure 4: Mesh sensitivity tests, showing normalised wall shear stress (left) and normalised velocity profiles along the gap (right) for the low-Re k-ε model (LS)

[2] $\overline{\tau_w}$ is the wall shear stress normalized by the average wall shear stress over the ±45° segment.

[3] U⁺ is the velocity normalised by the friction velocity, $u_\tau = \sqrt{\tau_w/\rho}$.

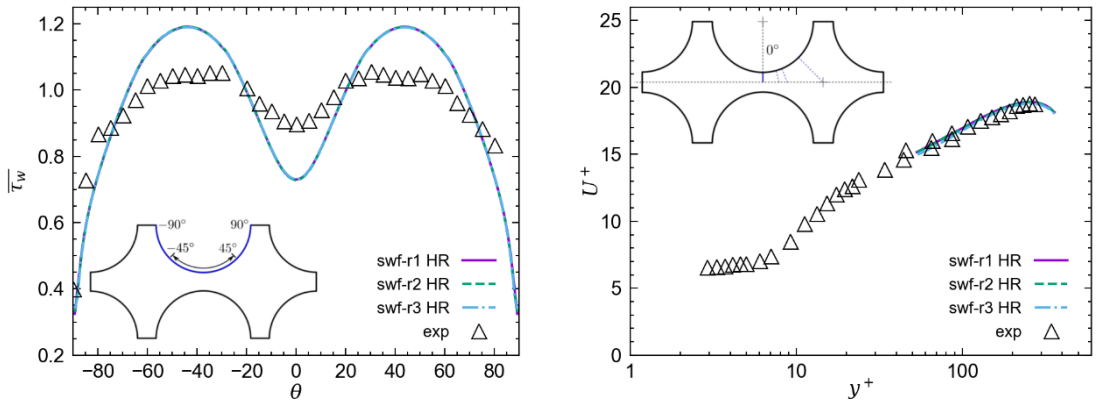

Figure 5: Mesh sensitivity tests, showing normalised wall shear stress (left) and normalised velocity profiles along the gap (right) for the high-Re k-ε model (HR).

4.2 Wall shear stress

Losses due to fluid friction against solid surfaces contribute significantly to the overall pressure loss, and thus thermal hydraulic performance, of the rod bundles within a nuclear fuel assembly. Accurate reproduction of the wall shear stress is required not only to increase accuracy in the calculation of this pressure loss, but also to ensure the near-wall behaviour of the flow is correctly computed, since the near-wall flow provides the main source of turbulent production and is responsible for the convective (and turbulent) transport of heat away from the walls.

Figure 6 and Figure 7 show predictions of the wall shear stress along the top rod surface for low-Re and wall function (high-Re) approaches respectively. Most models tested demonstrate good qualitative agreement with the experimental data, correctly reproducing the characteristic 'double hump'. In the low-Re approaches, the more advanced HJ RSM provides the best quantitative agreement, with the non-linear KS closure providing a small, but noticeable, improvement over the two linear EVMs (LS and FM).

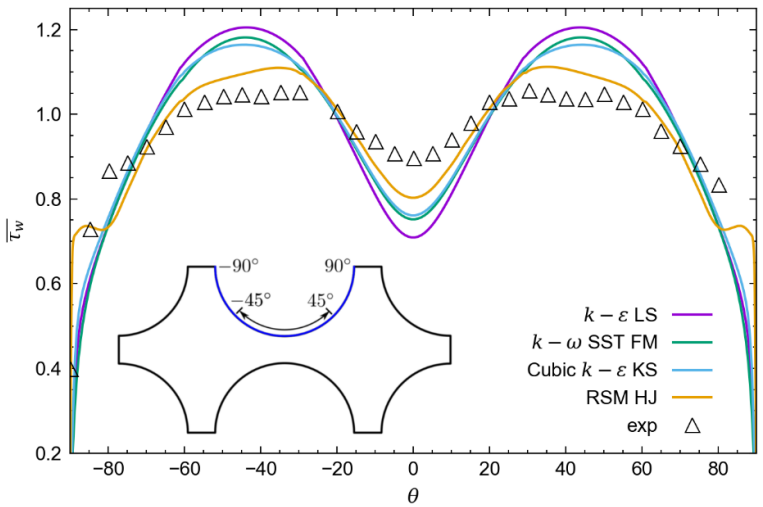

Figure 6 – Normalised wall shear stress as predicted by the low-Re turbulence models

In the high-Re approaches, the linear EVM (HR) provides results quantitatively similar to its low-Re counterparts, with the more advanced analytical wall function approach offering significant improvements. The two RSMs (GL and CL), however, display more curious behaviour. Here, significant dips in τ_w are predicted at ± 45° (where the perpendicular bisector of the rod wall intersects the sub-channel centre) and elevated levels of τ_w are seen at 0° within the rod gap. This behaviour can potentially be linked to the prediction of an additional secondary motion that the RSMs capture.

Whilst detection of the secondary motion was not the objective of Hooper's experiments (it is unclear if the resolution of the experiment was sufficient to capture it), there is some evidence in the experimental results of small dips at around ± 45° and evidence from other sources (see Sections 1 and 4.5) strongly suggests that secondary motion would have been present under the conditions studied. However, Figure 7 shows significant deviation from the experimental results when the RSM models are used in conjunction with standard wall functions. This finding highlights the limitations of the standard wall functions as the convection effects implied by the secondary flows are specifically ignored in the log-law formulation used. Since the analytical wall function solves a simplified momentum equation, it is capable of including such effects and therefore provides a better quantitative prediction. For the HR model and the two RSM models, use of an analytical wall function brings both the peaks and dips in Figure 7 closer to the experimental data, especially at 0°.

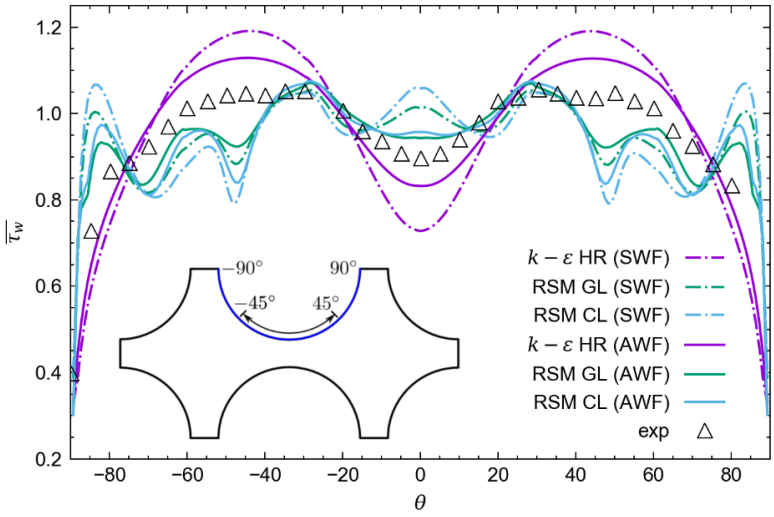

Figure 7: Normalised wall shear stress as predicted by high-Re turbulent models using standard (dashed) and analytical (solid) wall function approaches

4.3 Velocity profiles

Velocity profiles along the gap centre and at 45° away from the centre of the top middle rod are shown in Figure 8 for all models considered. In the gap centre agreement between the experimental data and the low-Re models is good, with the profile predicted by the HJ model slightly below the experimental data. This slight under prediction is also seen for the other low-Re models in the profile taken at 45° (Figure 8c), with exception of the k-ω SST (FM) which lies slightly above. Both of these differences are likely to be within the experimental error associated with the measurement points, but unfortunately this was not quantified by Hooper in the paper.

For the high-Re models on the right hand side of Figure 8, the standard wall function approach can be seen to over predict both profiles (0° and 45°) when used with the two RSMs. In both cases the AWF offers improvements, achieving excellent agreement for the profile at 0° (Figure 8b). At 45° some of the over prediction with the RSMs could be attributed to the under prediction in τ_w in this region, since U^+ is scaled by the friction velocity (and thus essentially $\sqrt{\tau_w}$), but this is not entirely consistent with the predictions shown along the 0° line (where an over prediction of τ_w did not lead to an under prediction in U^+) . However, since a) a comparison between the low-Re RSM and EVM approaches (on the left of Figure 8) indicates that the effects of the secondary motion on the axial velocity profile are generally small and b) the high-Re EVM approach gave generally good agreement, the discrepancies shown by the high-Re RSMs can probably be attributed towards interactions between the secondary motion (however small) and the wall function formulation.

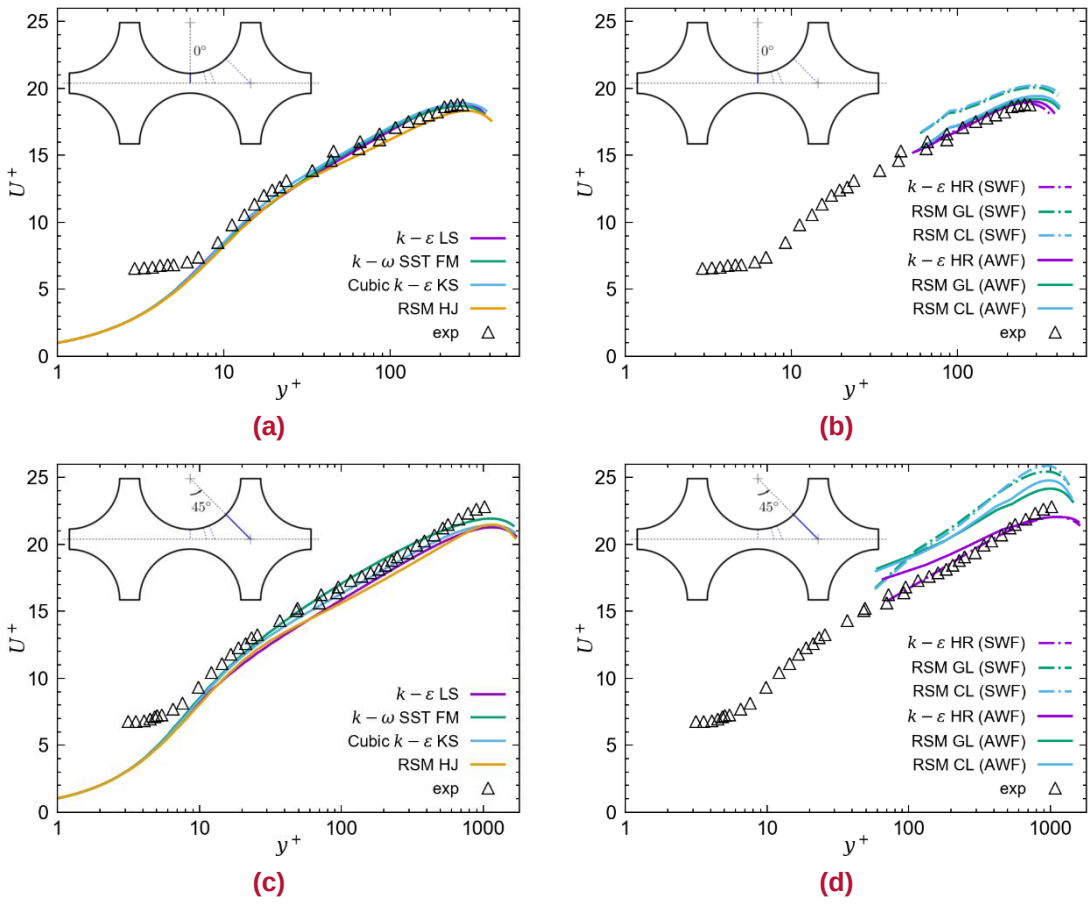

Figure 8: Normalised velocity profiles along the gap centre (top) and at 45° away from the centre of the top rod (bottom), indicated inset, for low-Re models (left) and high-Re models (right)

4.4 Turbulent shear stress

Physically, the turbulence in this kind of flow will promote mixing, not just of momentum but also anything else transported by the flow, including heat. In a wall-bounded flow, such as the sub-channel under consideration here, the dominance of the wall-normal gradients over wall-parallel ones ensures that the turbulent shear component forms a leading order term in the mean axial

momentum equation. It is thus the primary means by which the effects of the turbulence on the mean flow are accounted for. The correct reproduction of the turbulent shear stress thus forms a key modelling objective.

Figure 9 shows the predictions of the turbulent shear stress ($\overline{uv}$) along the gap centre and at 45° away from the centre of the top middle rod. The low-Re models again provide excellent agreement along the gap centre (0°) with some slight deviations in shape shown for the profile at 45°. Here, all models deviate below the experimental data just after the near-wall peak. The HJ RSM is the least affected and provides the best quantitative agreement. The other models all under predict the gradient of $\overline{uv}$, leading to an over prediction towards the sub-channel centre.

With the wall function approach there is clearly less consistency between the various models employed. Along the rod gap (0°) the AWF again offers improvements for both RSMs tested but slightly reduces agreement for the HR k-ε. The discrepancies at the start of the profiles (close to the wall) are most likely due to large changes in the wall-normal cell size, which result from the mesh requirements imposed by the wall function approach. At 45°, and excluding the start, the RSMs provide generally good agreement with the experimental data with little difference seen between the AWF and SWF approach. The HR eddy-viscosity model shows more erratic behaviour, initially producing a significant under prediction before recovering to provide an over prediction towards the sub-channel centre.

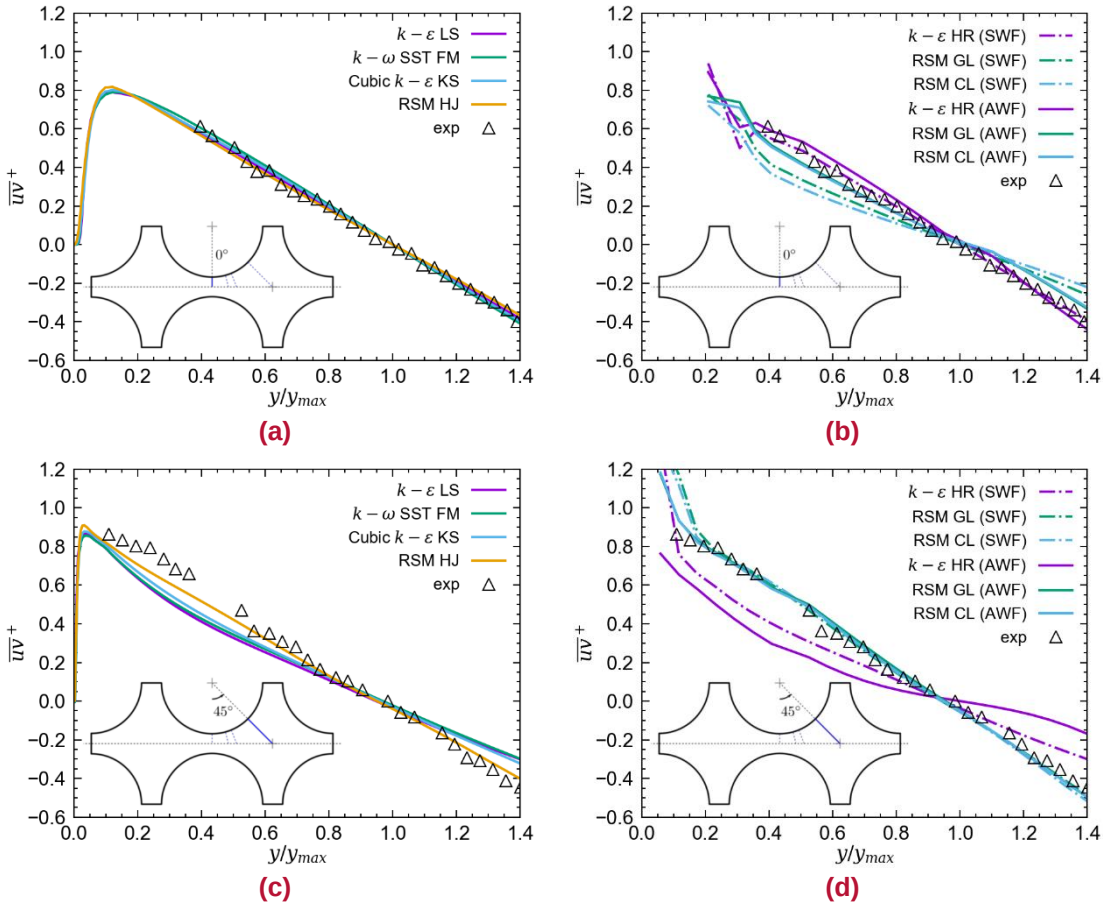

Figure 9: Normalised turbulent shear stress ($\overline{uv}^+ = \overline{uv}/\tau_w$) profiles along the gap centre (top) and at 45° away from the centre of the top rod (bottom), indicated inset, for low-Re models (left) and high-Re models (right)

4.5 Secondary motion

One defining aspect of the sub-channel type flows, as discussed in Section 1, is the presence of secondary motion. As this is driven by anisotropy in the Reynolds stresses, only those models capable of producing anisotropy are expected to be able to correctly reproduce it. Despite their small magnitude compared with the mean axial flow (typically only 1-2%), secondary flows are important since they provide an additional mixing mechanism within the sub-channel. Though thermal effects have not been directly considered in this report, previous studies have shown that the existence of the secondary flow directly affects the circumferential distribution of the rod wall outer surface temperature (EPRI 2014). Whilst, unfortunately, Hooper was unable to accurately directly measure the secondary motion present, owing to its small magnitude, the discussion in the paper does infer its presence from other results.

Figure 10 visualises the secondary motion predicted by the cubic k-ε model (KS, top half) and the HJ RSM (bottom half) by superimposing streamlines over contours of the axial velocity for one of the sub-channels. The secondary motion comprises a number of counter-rotating cells, which tend to move fluid from the channel centre towards the boundaries furthest away (that is, not towards the closer rod wall). Once the flow reaches these boundaries it follows the rod surface until meeting the adjacent cell at 45°. It then returns towards the centre of the channel completing the circulation. Some black arrows have been added to the streamlines to better illustrate the direction of the cells. The non-linear EVM captures the secondary cells quite well though the magnitude of the motion (0.32% of mean axial) was noticeably less than that predicted by the RSM (2.1% of mean axial). As expected, none of the linear EVM captured any secondary motion.

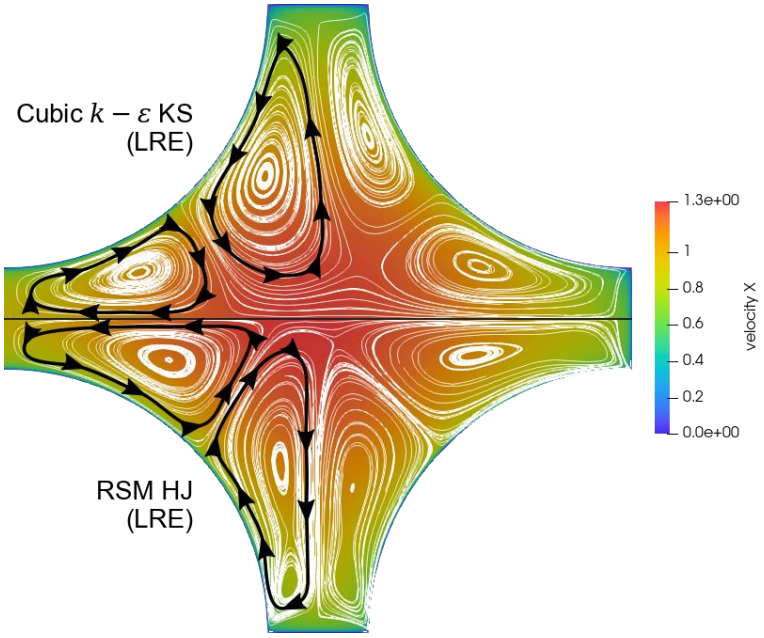

Figure 10: Velocity streamlines in the sub-channel cross-section superimposed over contours of the axial velocity. Only one sub-channel has been plotted, with the top half showing results from the cubic non-linear k-ε (KS) and the bottom half showing results from the HJ RSM.

Whilst the magnitude of the secondary motion is evidently only small, it is known to alter the distribution of axial velocity within a wide array of non-circular internal geometries (Meyer 2010).

Figure 11 illustrates this alteration by showing contours of the axial mean velocity for a number of the models considered in this work. To generate the figure, a contour of the upper left quadrant of the left sub-channel is created for each of the models compared. This is then rotated and shifted as necessary to reconstruct a full sub-channel, allowing predictions of axial velocity to be more easily compared. Contour lines (in black) have also been added to help illustrate the differences.

The two linear EVM (LS and FM), shown in the upper half of Figure 11a, return largely similar velocity contours, with the inner most contour line being almost circular. The HJ RSM predicts the curvature of this contour line to be significantly reduced; a direct result of the (now captured) secondary motion moving fluid towards the centre along the 45° normal, as indicated previously by Figure 10. Though, as also indicated by Figure 10, the non-linear EVM is able to qualitatively reproduce the correct effect, the reduced magnitude offers only a small, but still noticeable, alteration to the axial velocity distribution. In Figure 11b, the different wall treatments are compared for two of the high-Re turbulence models considered (HR and GL), where it can be seen that the analytical wall function provides only minor differences to the axial velocity distribution when used with the HR k-ε model. There are some noticeable improvements when used with the GL RSM, however, where the small deformations in the near-wall velocity contours predicted by the standard wall function can be seen to be reduced.

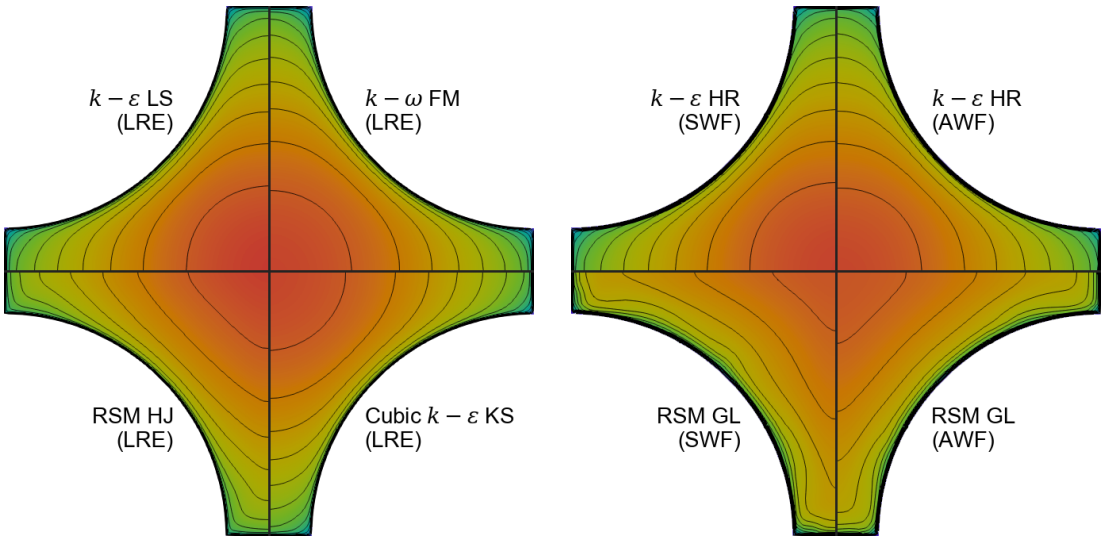

Figure 11: Contours of axial velocity in the sub-channel cross-section, where the results from the models indicated are plotted in one "quadrant" and placed next to each other for comparison. The upper left quadrant in the left sub-channel has been plotted, rotated as necessary, for each model to ensure fair comparison.

5 Discussion and Conclusions

This report presents CFD simulations of the flow through a square-arrayed twin sub-channel geometry typical of those found in nuclear thermal hydraulic applications. A wide range of turbulence models (linear eddy-viscosity, non-linear eddy-viscosity and stress transport) have been applied and the use of different near-wall treatments (low-Re and wall functions) has also been considered. The simulations reproduce the experimental results published by Hooper (1980) and the analysis provides an appraisal of the various modelling approaches tested.

For those models which can capture turbulence anisotropy, predictions of the wall shear stress revealed significant qualitative differences between the two near-wall modelling approaches applied. Both high-Re Reynolds stress models tested (Gibson-Launder, GL, and Craft-Launder, CL) predicted wall shear stress profiles which deviated from the experimental data at locations on the rod surface where effects from secondary motion were present. Owing to its ability to include convection and pressure-gradient effects, the more advanced analytical wall function approach offered better quantitative agreement, though did not remove the deviations entirely. All the low-Re models tested, including the EVMs, offered qualitatively correct results, with the full stress transport closure of Hanjalić & Jakirlić (HJ) providing the best quantitative agreement. Comparisons of velocity and turbulent shear stress supported these conclusions, with the low-Re near-wall modelling approach offering generally better agreement. The analytical wall function was again seen to offer improvements in some cases.

Whilst 'secondary motion' was not directly measured by Hooper, its presence was inferred within the paper and can be assumed from a large body of existing literature on flows through similar cross-sections. As expected, the linear eddy-viscosity models tested could not reproduce the secondary motion and thus failed to capture the deformation in the distribution of mean axial velocity this produces within the sub-channel cross-section. The cubic non-linear eddy-viscosity model tested (Craft-Suga, KS) did correctly reproduce the secondary circulation cells, though the magnitude of the motion was an order of magnitude less than that produced by the RSMs.

Overall, a number of key conclusions can be drawn from this work:

- Low-Re models demonstrated consistently better overall performance, due to their superior ability in reproducing the correct near-wall behaviour. They are recommended over high-Re approaches if computational resources allow.
- The more advanced low-Re HJ RSM offered the best quantitative agreement out of all the models tested.
- If a low-Re near-wall approach is not computationally feasible, then analytical wall functions offer noticeable improvements over standard wall functions, owing to their ability to account for near-wall convection and pressure gradient effects.
- In sub-channel flows of this type, secondary flows can produce noticeable alterations in the mean axial velocity distribution and would be likely to affect the heat transfer from the fuel. Approaches based on the linear eddy-viscosity formulation cannot capture this, owing to their inability to account for anisotropy in the Reynold stresses; ideally a stress transport approach is required.
- Standard wall functions should be used with caution when used in conjunction with turbulence models that can reproduce secondary flows, since the resulting near-wall velocity may not necessarily fit a standard log-law. In the case studied in this report, use of the standard wall functions produced predictions that differed significantly from the experimental results.

- Models have been assessed against detailed data which was openly available and obtained from a suitably simple geometry. There is a clear need for more openly available high-quality ‘CFD-grade’ experimental and numerical datasets for flows relevant to nuclear thermal hydraulics that would allow more thorough testing and assessment.

In summary, the results demonstrate both the deficiencies of the standard wall function approach in reproducing flows with significant near-wall convection and pressure-gradient effects, and the limitations of using linear eddy-viscosity approaches in flows with significant anisotropic effects.

Whilst the superiority of the low-Re near-wall approach is clear for the flow studied in this case, for higher Reynolds number flow, such as would be seen in a PWR under normal operation, it is likely that a full low-Re approach would demand an unfeasibly fine mesh in the near-wall region. However, the overall impact of not resolving the viscosity affected near-wall region (i.e. by using a wall function approach) may be reduced, since the viscous layer becomes much thinner. The analytical wall function tested here does demonstrate significant improvements over the standard ‘log-law’ based formulation and is thus recommended if computational resources do not allow a full low-Re approach.

6 References

Biemüller, M., Meyer, L., & Rehme, K. (1996). Large eddy simulation and measurement of the structure of turbulence in two rectangular channels connected by a gap. In *Engineering Turbulence Modelling and Experiments, Volume 3*, Elsevier, pp. 249–258.

Brundrett, E., & Baines, W. D. (1964). The production and diffusion of vorticity in duct flow. *Journal of Fluid Mechanics*, **19**(3), 375–394.

Conner, M. E., Baglietto, E., & Elmahdi, A. M. (2010). CFD methodology and validation for single-phase flow in PWR fuel assemblies. *Nuclear Engineering and Design*, **240**(9), 2088–2095.

Craft, T. J., Gant, S. E., Gerasimov, A. V., Iacovides, H., & Launder, B. E. (2006). Development and application of wall-function treatments for turbulent forced and mixed convection flows. *Fluid Dynamics Research*, **38**(2–3), 127–144.

Craft, T. J., Gant, S. E., Iacovides, H., & Launder, B. E. (2004). A New Wall Function Strategy for Complex Turbulent Flows. *Numerical Heat Transfer, Part B: Fundamentals*, **45**(4), 301–318.

Craft, T. J., Gerasimov, A. V., Iacovides, H., & Launder, B. E. (2002). Progress in the generalization of wall-function treatments. *International Journal of Heat and Fluid Flow*, **23**(2), 148–160.

Craft, T. J., & Launder, B. E. (1992). New Wall-Reflection Model Applied to the Turbulent Impinging Jet. *AIAA Journal*, **30**(12), 2970–2972.

Craft, T., Launder, B., & Suga, K. (1996). Development and application of a cubic eddy-viscosity model of turbulence. *International Journal of Heat and Fluid Flow*, **17**(2), 108–115.

Daly, B. J., & Harlow, F. H. (1970). Transport Equations in Turbulence. *Physics of Fluids*, **13**(11), 2634–2649.

Duan, Y., & He, S. (2017). Large eddy simulation of a buoyancy-aided flow in a non-uniform channel – Buoyancy effects on large flow structures. *Nuclear Engineering and Design*, **312**, 191–204.

EPRI. (2014). *Computational Fluid Dynamics Benchmark of High Fidelity Rod Bundle Experiments* (Technical Report No. 3002000504), Electric Power Research Institute.

Gerasimov, A. V. (2004). *Development and validation of an analytical wall-function strategy for modelling forced, mixed and natural convection flows* (Ph.D.), University of Manchester : UMIST. Retrieved from https://ethos.bl.uk/OrderDetails.do;jsessionid=A7E74FACE751A8EB1722E9BBF420A551?uin=uk.bl.ethos.488407

Gessner, F. B., & Jones, J. B. (1965). On some aspects of fully-developed turbulent flow in rectangular channels. *Journal of Fluid Mechanics*, **23**(4), 689–713.

Gibson, M., & Launder, B. E. (1978). Ground Effects on Pressure Fluctuations in the Atmospheric Boundary Layer. *Journal of Fluid Mechanics*, **86**(03), 491–511.

Hanjalić, K., & Jakirlić, S. (1993). A model of stress dissipation in second-moment closures. *Applied Scientific Research*, **51**(1–2), 513–518.

Hanjalić, K., Jakirlić, S., & Durst, F. (1994). A computational study of joint effects of transverse shear and streamwise acceleration on three-dimensional boundary layers. *International Journal of Heat and Fluid Flow*, **15**(4), 269–282.

Hanjalić, K., Jakirlić, S., & Hadžić, I. (1997). Expanding the limits of “equilibrium” second-moment turbulence closures. *Fluid Dynamics Research*, **20**(1–6), 25–41.

Hoagland, L. C. (1962). *Fully developed turbulent flow in straight rectangular ducts : secondary flow, its cause and effect on the primary flow* (Thesis), Massachusetts Institute of Technology. Retrieved from http://dspace.mit.edu/handle/1721.1/44470

Hooper, J. D. (1980). Developed single phase turbulent flow through a square-pitch rod cluster. *Nuclear Engineering and Design*, **60**(3), 365–379.

Huser, A., & Biringen, S. (1993). Direct numerical simulation of turbulent flow in a square duct. *Journal of Fluid Mechanics*, **257**, 65–95.

Ikeno, T., & Kajishima, T. (2010). Analysis of dynamical flow structure in a square arrayed rod bundle. *Nuclear Engineering and Design*, **240**(2), 305–312.

Jakirlić, S., & Hanjalić, K. (1995). A second-moment closure for non-equilibrium and separating high- and low-Re-number flows. In *10th Symposium on Turbulent Shear Flows*, Pennsylvania State University, pp. 23–30.

Jakirlic, S., Hanjalic, K., & Tropea, C. (2002). Modeling Rotating and Swirling Turbulent Flows: A Perpetual Challenge. *AIAA Journal*, **40**(10), 1984–1996.

Launder, B. (1975). On the effects of a gravitational field on the turbulent transport of heat and momentum. *Journal of Fluid Mechanics*, **67**(03), 569–581.

Launder, B., Reece, G. J., & Rodi, W. (1975). Progress in the development of a Reynolds-stress turbulence closure. *Journal of Fluid Mechanics*, **68**(03), 537–566.

Launder, B., & Sharma, B. (1974). Application of the energy-dissipation model of turbulence to the calculation of flow near a spinning disc. *Letters in Heat and Mass Transfer*, **1**(2), 131–137.

Launder, B., & Spalding, D. (1974). The numerical computation of turbulent flows. *Computer Methods in Applied Mechanics and Engineering*, **3**(2), 269–289.

Laurence, D., Iacovides, H., Craft, T. J., … Liu, B. (2019). *Project FORTE - Nuclear Thermal Hydraulics Research and Development - Critical Review of State-of-the-Art Thermal Hydraulic Prediction Capability,* FNC 53798/46733R, Issue 1.

Lien, F., & Leschziner, M. (1994a). A general non-orthogonal collocated finite volume algorithm for turbulent flow at all speeds incorporating second-moment turbulence-transport closure, Part 1: Computational implementation. *Computer Methods in Applied Mechanics and Engineering*, **114**(1–2), 123–148.

Lien, F., & Leschziner, M. (1994b). Upstream monotonic interpolation for scalar transport with application to complex turbulent flows. *International Journal for Numerical Methods in Fluids*, **19**(6), 527–548.

Mayer, G., & Házi, G. (2006). Direct numerical and large eddy simulation of longitudinal flow along triangular array of rods using the lattice Boltzmann method. *Mathematics and Computers in Simulation*, **72**(2), 173–178.

Menter, F. R. (1994). Two-equation eddy-viscosity turbulence models for engineering applications. *AIAA Journal*, **32**(8), 1598–1605.

Meyer, L. (2010). From discovery to recognition of periodic large scale vortices in rod bundles as source of natural mixing between subchannels—A review. *Nuclear Engineering and Design*, **240**(6), 1575–1588.

Meyer, L., & Rehme, K. (1994). Large-scale turbulence phenomena in compound rectangular channels. *Experimental Thermal and Fluid Science*, **8**(4), 286–304.

Naot, D., Shavit, A., & Wolfshtein, M. (1970). Interactions between components of the turbulent velocity correlation tensor due to pressure fluctuations. *Israel Journal of Technology*, **8**(3), 259–269.

Prandtl, L. (1952). Essentials of Fluid Dynamics. *Received 4 March 1980*.

Rehme, K. (1987). The structure of turbulent flow through rod bundles. *Nuclear Engineering and Design*, **99**(Supplement C), 141–154.

Rotta, J. (1951). Statistische Theorie nichthomogener Turbulenz. *Zeitschrift Fur Physik*, **129**, 547–572.

Rowe, D. S., Johnson, B. M., & Knudsen, J. G. (1974). Implications concerning rod bundle crossflow mixing based on measurements of turbulent flow structure. *International Journal of Heat and Mass Transfer*, **17**(3), 407–419.

Shir, C. C. (1973). A Preliminary Numerical Study of Atmospheric Turbulent Flows in the Idealized Planetary Boundary Layer. *Journal of the Atmospheric Sciences*, **30**(7), 1327–1339.

Wells, D. M., Peturaud, P., & Yagnik, S. K. (2016). Overview of CFD Round Robin Benchmark of the High Fidelity Fuel Rod Bundle NESTOR Experimental Data. In *Proceedings of the 16th International Topical Meeting on Nuclear Thermal Hydraulics*, Vol. 1, Chicago, pp. 627–639.

Wilcox, D. (1988). Reassessment of the scale-determining equation for advanced turbulence models. *AIAA Journal*, **26**(11), 1299–1310.

Wilcox, D. C. (2008). Formulation of the k-w Turbulence Model Revisited. *AIAA Journal*, **46**(11), 2823–2838.

ANNEX A - NUMERICAL MODELS

A1 Turbulence models

This section provides a brief, but complete, description of the turbulence models used in this work. For further details, the reader is referred to the original papers where the models were presented (as listed in Table 2).

A.1.1 Eddy-viscosity models

For models based on the linear eddy-viscosity concept $\overline{u_i u_j}$ is written as:

$$\overline{u_i u_j} = \frac{2}{3} k \delta_{ij} - 2\nu_t S_{ij} \quad (3)$$

where ν_t, the turbulent viscosity, takes a form specific to the model. The strain rate tensor S_{ij} is defined as:

$$S_{ij} = \frac{1}{2}\left(\frac{\partial U_i}{\partial x_j} + \frac{\partial U_j}{\partial x_i}\right) \quad (4)$$

A.1.1.1 k-ε models

The two-equation k-ε models solve transport equations for the turbulent kinetic energy k and the dissipation rate ε. These can be written, in generic form, as:

$$\frac{\partial k}{\partial t} + U_i \frac{\partial k}{\partial x_i} = \frac{\partial}{\partial x_i}\left[\left(\nu + \frac{\nu_t}{\sigma_k}\right)\frac{\partial k}{\partial x_i}\right] + P_k - \varepsilon - D \quad (5)$$

$$\frac{\partial \varepsilon}{\partial t} + U_i \frac{\partial \varepsilon}{\partial x_i} = \frac{\partial}{\partial x_i}\left[\left(\nu + \frac{\nu_t}{\sigma_\varepsilon}\right)\frac{\partial \varepsilon}{\partial x_i}\right] + (C_{\varepsilon 1} f_{\varepsilon 1} P_k - C_{\varepsilon 2} f_{\varepsilon 2} \varepsilon)\frac{\varepsilon}{k} + S_\varepsilon \quad (6)$$

where the terms $f_{\varepsilon 1}$, $f_{\varepsilon 2}$, D and S_ε represent the near-wall damping modifications added by low-Re models. σ_k, σ_ε, $C_{\varepsilon 1}$ and $C_{\varepsilon 2}$ are model constants. The eddy viscosity takes the form:

$$\nu_t = C_\mu f_\mu \frac{k^2}{\varepsilon} \quad (7)$$

where c_μ is a constant and f_μ is a near-wall damping term. The production term, P_k, is exact and requires no modelling:

$$P_k = -\overline{u_i u_j}\frac{\partial U_i}{\partial x_j} \quad (8)$$

The low-Re Launder-Sharma model considered in this work transports $\tilde{\varepsilon}$, the so-called homogeneous dissipation rate, rather than ε since $\tilde{\varepsilon}$ conveniently goes to zero at a wall. The correct form of Equation 6 can be obtained simply by replacing ε with $\tilde{\varepsilon}$ since the additional D term accounts for the difference. Model coefficients and low-Re damping terms for the two k-ε models used in this work are presented in Table 3 and Table 4 respectively.

Model	C_μ	$C_{\varepsilon 1}$	$C_{\varepsilon 2}$	σ_k	σ_ε
HR, LS	0.09	1.44	1.92	1.0	1.3

Table 3: Model coefficients for k-ε models

Model	f_μ	D	$f_{\varepsilon 1}$	$f_{\varepsilon 2}$	S_ε
HR	1	0	1	1	1
LS	$\exp\left[\frac{-3.4}{(1+R_t/50)^2}\right]$	$2\nu\left(\frac{\partial\sqrt{k}}{\partial x_i}\right)^2$	1	$1-0.22e^{-(R_t/6)^2}$	$2\nu\nu_t\left(\frac{\partial^2 U_i}{\partial x_j \partial x_k}\right)^2$

Table 4: Viscous damping terms and functions for k-ε models (turbulent Reynolds number $R_t = k^2/\nu\tilde{\varepsilon}$)

A.1.1.2 k-ω SST model

k-ω type models solve a transport equation for ω, the specific dissipation rate ($\omega \equiv \varepsilon/k$) as its scale determining equation. One such model is the k-ω SST of (Menter 1994), which is a hybrid model that essentially blends a k-ε type model in the far-field with a k-ω model near the wall through the use of a blending function. It can be applied all the way down to the viscous sublayer without any additional modification. The k equation is of similar form to Equation 5,

$$\frac{\partial k}{\partial t} + U_i\frac{\partial k}{\partial x_i} = \frac{\partial}{\partial x_i}\left[\left(\nu + \frac{\nu_t}{\sigma_k}\right)\frac{\partial k}{\partial x_i}\right] + P_k - \beta\omega k \quad (9)$$

$$\frac{\partial \omega}{\partial t} + U_i\frac{\partial \omega}{\partial x_i} = \frac{\partial}{\partial x_i}\left[\left(\nu + \frac{\nu_t}{\sigma_\omega}\right)\frac{\partial \omega}{\partial x_i}\right] + \frac{\gamma}{\nu_t}P_k - \beta\omega^2 + 2(1-f_{\omega 1})C_{\omega 1}\frac{1}{\omega}\frac{\partial k}{\partial x_i}\frac{\partial \omega}{\partial x_i} \quad (10)$$

where γ and β are model coefficients and the production term P_k is as per Equation 8. The final term in Equation 10 represents a cross-diffusion term which is notably absent from the original k-ω proposed by (Wilcox 1988)[4]. The blending function $f_{\omega 1}$ is defined as:

$$f_{\omega 1} = \tanh(\Upsilon_1^4) \quad (11)$$

$$\Upsilon_1 = \min\left[\max\left(\frac{\sqrt{k}}{\beta^*\omega y_n}, \frac{500\nu}{y_n^2\omega}\right), \frac{2k\omega}{D_{k\omega}}\right] \quad (12)$$

$$\mathrm{D_{k\omega}} = \max\left[\frac{\partial k}{\partial x_i}\frac{\partial \omega}{\partial x_i}, 0\right] \quad (13)$$

where β^* is a model coefficient and y_n is the distance from the nearest wall.

The eddy viscosity is taken as:

$$\nu_t = \frac{\alpha^* k}{\min[\alpha^*\omega, |\omega| f_{\omega 2}]} \quad (14)$$

where a_1 is a model coefficient. The function $f_{\omega 2}$ is:

$$f_{\omega 2} = \tanh(\Upsilon_2^4) \quad (15)$$

$$\Upsilon_2 = \max\left[\frac{2\sqrt{k}}{\beta^*\omega y_n}, \frac{500\nu}{y_n^2\omega}\right] \quad (16)$$

Model coefficients can be found in Table 5, where the final coefficients are formed, for any coefficient ϕ, by taking $\phi = f_{\omega 1}\phi_1 + (1-f_{\omega 1})\phi_2$. The coefficient γ is defined as:

$$\gamma = \gamma_1 f_{\omega 1} + (1-f_{\omega 1})\gamma_2 \quad (17)$$

$$\gamma_1 = \frac{\beta_1}{\beta^*} - \frac{\sigma_{\omega 1}\kappa^2}{\sqrt{\beta^*}}, \quad \gamma_2 = \frac{\beta_2}{\beta^*} - \frac{\sigma_{\omega 2}\kappa^2}{\sqrt{\beta^*}} \quad (18)$$

[4] Though it was added as a later modification by Wilcox (2008).

where $\kappa = 0.41$.

Model		α^*	β^*	α	β	σ_k	σ_w
FM	ϕ_1	0.31	0.09	0.553	0.075	0.85	0.5
	ϕ_2	0.31	0.09	0.440	0.083	1.0	0.856

Table 5: Model coefficients for the *k-w* SST. The coefficients are formed as $\phi = f_{\omega 1}\phi_1 + (1 - f_{\omega 1})\phi_2$

A.1.1.3 Cubic non-linear k-ε model

Non-linear eddy-viscosity models extend the linear stress-strain relationship of Boussinesq (Equation 3) by supposing that a more generalized relationship might exist between the Reynolds stresses and mean strains:

$$\overline{u_i u_j} = \frac{2}{3}k\delta_{ij} - 2\nu_t S_{ij} + f(S_{ij}, \Omega_{ij}) \quad (19)$$

where f is any non-linear function of S_{ij} and Ω_{ij}, and Ω_{ij} is the mean rotation rate tensor:

$$\Omega_{ij} = \frac{1}{2}\left(\frac{\partial U_i}{\partial x_j} - \frac{\partial U_j}{\partial x_i}\right) \quad (20)$$

One such model proposed by Craft *et al.* (1996) introduces a cubic stress-strain relationship. First, Equation 19 is reformulated in terms of the anisotropy tensor, a_{ij}:

$$a_{ij} \equiv \frac{\overline{u_i u_j}}{k} - \frac{2}{3}\delta_{ij} \quad (21)$$

The model then proposes:

$$\begin{aligned} a_{ij} = -2\frac{\nu_t}{k}S_{ij} &+ C_1\frac{\nu_t}{\tilde{\varepsilon}}\left(S_{ik}S_{jk} - \frac{1}{3}S_{kl}S_{kl}\delta_{ij}\right) \\ &+ 4C_2\frac{\nu_t}{\tilde{\varepsilon}}\left(\Omega_{ik}S_{jk} - \Omega_{jk}S_{ik}\right) \\ &+ 4C_3\frac{\nu_t}{\tilde{\varepsilon}}\left(\Omega_{ik}\Omega_{jk} - \frac{1}{3}\Omega_{kl}\Omega_{kl}\delta_{ij}\right) \\ &+ 8C_4\frac{\nu_t k}{\tilde{\varepsilon}^2}\left(S_{ki}\Omega_{lj} + S_{kj}\Omega_{li}\right)S_{kl} + 8C_5\frac{\nu_t k}{\tilde{\varepsilon}^2}S_{ij}S_{kl}S_{kl} \\ &+ 8C_6\frac{\nu_t k}{\tilde{\varepsilon}^2}S_{ij}\Omega_{kl}\Omega_{kl} \end{aligned} \quad (22)$$

where $C_1 \ldots C_6$ are model coefficients detailed in Table 6.

Model	C_1	C_2	C_3	C_4	C_5	C_6
KS	-0.1	0.1	0.26	$-10C_\mu^2$	$-5C_\mu^2$	$5C_\mu^2$

Table 6: Model coefficients for Equation 22, where C_μ is defined as per Equation 23

The turbulent viscosity is defined as per Equation 7, with C_μ and f_μ defined as:

$$C_\mu = \frac{0.3}{1 + 0.35\eta^{1.5}}\left\{1 - \exp\left[\frac{-0.36}{\exp(-0.75\eta)}\right]\right\} \quad (23)$$

$$f_\mu = 1 - \exp\left[-\left(\frac{R_t}{90}\right)^{0.5} - \left(\frac{R_t}{400}\right)^2\right] \quad (24)$$

where $R_t \equiv k^2/\nu\tilde{\varepsilon}$. η is defined as $\eta = \max(\tilde{S}, \tilde{\Omega})$, where $\tilde{S}$ and $\tilde{\Omega}$ are the dimensionless strain and vorticity invariants defined by:

$$\tilde{S} = \frac{k}{\tilde{\varepsilon}}\sqrt{2S_{ij}S_{ij}} \quad (25)$$

$$\widetilde{\Omega} = \frac{k}{\tilde{\varepsilon}}\sqrt{2\Omega_{ij}\Omega_{ij}} \quad (26)$$

The transport equations for k and ε are the same as those given by Equation 5 and 6, and the coefficients $C_{\varepsilon 1}$, $C_{\varepsilon 2}$, σ_ε, σ_k, and the functions f_1, f_2 are the same as those for the LS model given in Table 3 and Table 4 respectively. The near wall source term, S_ε, is modified to be:

$$S_\varepsilon = \begin{cases} 0.0022\dfrac{\tilde{S}\nu_t k^2}{\tilde{\varepsilon}}\left(\dfrac{\partial^2 U_i}{\partial x_j \partial x_k}\right)^2, & \tilde{R}_t \leq 250 \\ 0, & \tilde{R}_t > 250 \end{cases} \quad (27)$$

A.1.2 Reynolds Stress Models

Even with the additional of non-linear terms, the Boussinesq stress-strain relationship is often cited as one of the major weaknesses of eddy-viscosity models. Reynolds stress models entirely avoid the need to specify a constitutive stress-strain relationship by solving additional transport equations for each component of $\overline{u_i u_j}$. These can be written, in exact form, as:

$$\frac{\partial \overline{u_i u_j}}{\partial t} + U_i \frac{\partial \overline{u_i u_j}}{\partial x_i} = P_{ij} - \varepsilon_{ij} + \Phi_{ij} - D_{ij} \quad (28)$$

where

$$P_{ij} = -\left(\overline{u_i u_k}\frac{\partial U_j}{\partial x_k} + \overline{u_j u_k}\frac{\partial U_i}{\partial x_k}\right) \quad (29)$$

$$\varepsilon_{ij} = 2\nu\overline{\frac{\partial u_i}{\partial x_k}\frac{\partial u_i}{\partial x_k}} \quad (30)$$

$$\Phi_{ij} = \overline{\frac{p}{\rho}\left(\frac{\partial u_j}{\partial x_j} + \frac{\partial u_i}{\partial x_j}\right)} \quad (31)$$

$$D_{ij} = \frac{\partial}{\partial x_k}\left[\overline{u_i u_j u_k} + \overline{\frac{p}{\rho}\left(u_j\delta_{ik} + u_i\delta_{jk}\right)} - \nu\frac{\partial \overline{u_i u_j}}{\partial x_k}\right] \quad (32)$$

are terms representing production, viscous dissipation, pressure-strain and diffusion of $\overline{u_i u_j}$.

One of the major strengths of the RSM modelling approach is that the production terms, P_{ij}, are exact and do not require modelling. They also reveal an additional mechanism which acts on the Reynolds stresses, represented by the pressure-strain term Φ_{ij}, which is traceless and thus does not appear in any equation that transports k. Although this term does requiring modelling, it nonetheless means an RSM can at least in principle account for its effects. Most approaches begin by splitting Φ_{ij} into several parts, each reflecting a distinct physical interaction which is thought to contribute:

$$\Phi_{ij} = \Phi_{ij}^{(1)} + \Phi_{ij}^{(2)} + \Phi_{ij}^{(w)} \quad (33)$$

The specific closures used for this work are detailed in Sections A.1.2.1 and A.1.2.2.

A.1.2.1 Gibson & Launder (1978) Basic Closure

The basic second-moment closure model is formed from contributions by Rotta (1951), Launder & Sharma (1974), Launder *et al.* (1975), Launder (1975) and Gibson & Launder (1978). The slow pressure-strain term, $\Phi_{ij}^{(1)}$, is modelled following Rotta (1951):

$$\Phi_{ij}^{(1)} = -C_1\frac{\varepsilon}{k}\left(\overline{u_i u_j} - \frac{1}{3}\delta_{ij}\overline{u_k u_k}\right) \quad (34)$$

The rapid pressure-strain term, $\Phi_{ij}^{(2)}$, follows the *isotropization-of-production* model of Naot *et al.* (1970):

$$\Phi_{ij}^{(2)} = -C_2\left(P_{ij} - \frac{1}{3}\delta_{ij}P_{kk}\right) \quad 35$$

The $\Phi_{ij}^{(w)}$ provides the necessary corrections to both parts of the Φ_{ij} term (i.e. $\Phi_{ij}^{(1)}$, $\Phi_{ij}^{(2)}$) to account for the presence of a wall or free-surface. Thus, this term is split in an analogous fashion, such that

$$\Phi_{ij}^{(w)} = \Phi_{ij}^{(w,1)} + \Phi_{ij}^{(w,2)} \quad 36$$

The $\Phi_{ij}^{(w,1)}$ term is modelled following Shir (1973):

$$\Phi_{ij}^{(w,1)} = C_1^w \frac{\varepsilon}{k}\left(\overline{u_k u_l}n_l n_k \delta_{ij} - \frac{3}{2}\overline{u_i u_k}n_j n_k - \frac{3}{2}\overline{u_j u_k}n_i n_k\right) f_w \quad 37$$

where n_i is the ith component of the wall normal vector, $C_1^w = 0.5$ and f_w is an empirical function that varies from unity at the wall to zero far enough away;

$$f_w = \frac{k^{3/2}}{2.5\varepsilon y_n} \quad 38$$

where y_n is the normal distance from the wall. The second part to the wall correction is modelled as per Gibson & Launder (1978);

$$\Phi_{ij}^{(w,2)} = C_2^w\left(\Phi_{kl}^{(2)}n_l n_k \delta_{ij} - \frac{3}{2}\Phi_{ik}^{(2)}n_j n_k - \frac{3}{2}\Phi_{jk}^{(2)}n_i n_k\right) f_w \quad 39$$

The viscous dissipation term, ε_{ij}, is modelled as isotropic:

$$\varepsilon_{ij} = \frac{2}{3}\varepsilon\delta_{ij} \quad 40$$

where ε, the scalar dissipation rate, is obtained via a transport equation very similar in form to that used in the two-equation eddy-viscosity models described in Appendix A.1.1, the main difference being the utilization of the full second-moment forms of the production terms:

$$\frac{\partial \varepsilon}{\partial t} + U_k\frac{\partial \varepsilon}{\partial x_k} = \frac{\partial}{\partial x_k}\left[\left(\nu\delta_{kl} + C_\varepsilon\overline{u_k u_l}\frac{k}{\varepsilon}\right)\frac{\partial \varepsilon}{\partial x_l}\right] + \left(\frac{1}{2}C_{\varepsilon 1}f_1 P_{kk} - C_{\varepsilon 2}f_2\varepsilon\right)\frac{\varepsilon}{k} + S_\varepsilon \quad 41$$

where $C_\varepsilon = 0.18$, $C_{\varepsilon 1} = 1.44$ and $C_{\varepsilon 2} = 1.92$. Since this closure is for high-Re flows $S_\varepsilon = 0$.

For the diffusion term D_{ij}, the triple moments are modelled following the generalized gradient diffusion hypothesis of Daly & Harlow (1970) such that

$$\overline{u_i u_j u_k} = -C_s\frac{k}{\varepsilon}\overline{u_k u_l}\frac{\partial \overline{u_i u_j}}{\partial x_l} \quad 42$$

where $C_s = 0.2$. The part of D_{ij} containing the fluctuating pressure is assumed to be negligible.

A.1.2.2 Hanjalić & Jakirlić low-Re Closure

The Hanjalić & Jakirlić model aims to extend the applicability of the basic second-moment closure to those flows with significant low-Re and wall-proximity effects. It was proposed in a series of papers by (Hanjalić & Jakirlić (1993), Hanjalić et al. (1994) and Jakirlić & Hanjalić (1995). Amongst other changes it introductions a low-Re form of the ε transport equation, and makes the various coefficients in the $\overline{u_i u_j}$ equation functions of $\tilde{R}_t$ and the invariants of the stress and dissipations rate tensors (a_{ij} and e_{ij} respectively) . These invariants are introduced as:

$$A \equiv 1 - \frac{9}{8}(A_2 - A_3), \quad E \equiv 1 - \frac{9}{8}(E_2 - E_3) \tag{43}$$

where

$$A_2 \equiv a_{ij}a_{ij}, \quad A_2 \equiv a_{ij}a_{jk}a_{ki}, \quad E_2 \equiv e_{ij}e_{ij} \quad E_3 \equiv e_{ij}e_{jk}e_{ki} \tag{44}$$

The stress anisotropy tensor a_{ij} is as per Equation 21. The dissipation rate anisotropy tensor, e_{ij}, is defined as:

$$e_{ij} = \frac{\varepsilon_{ij}}{\varepsilon} - \frac{2}{3}\delta_{ij} \tag{45}$$

The linear pressure-strain terms of the basic closure are adopted for the slow, rapid and wall reflection terms (Equations 34, 35, 37 and 39 respectively), with the coefficients redefined as:

$$C_1 = C + \sqrt{A}E^2 \tag{46}$$

where

$$C = 2.5Af_A^{0.25}f_{\tilde{R}_t}, \quad f_A = \min[A_2, 0.6], \quad f_{\tilde{R}_t} = \min\left[\left(\frac{\tilde{R}_t}{150}\right)^{1.5}, 1\right] \tag{47}$$

$$C_2 = 0.8\sqrt{A} \tag{48}$$

$$C_1^w = \max[1 - 0.7C, 0.3] \tag{49}$$

$$C_2^w = \min[A, 0.3] \tag{50}$$

The model for the viscous dissipation rate tensor, ε_{ij}, is given as:

$$\varepsilon_{ij} = f_s\varepsilon_{ij}^* + (1 - f_s)\frac{2}{3}\varepsilon\delta_{ij} \tag{51}$$

where

$$\varepsilon_{ij}^* = \frac{\varepsilon}{k}\frac{\overline{u_iu_j} + \left(\overline{u_iu_k}n_jn_k - \overline{u_ju_k}n_in_k - \overline{u_ku_l}n_kn_ln_in_j\right)f_d}{1 + \frac{3}{2}\frac{u_iu_j}{k}n_pn_qf_d} \tag{52}$$

and

$$f_s = 1 - \sqrt{A}E^2, \quad f_d = \left(1 - 0.1\tilde{R}_t\right)^{-1} \tag{53}$$

The scalar dissipation rate, ε, is provided as per Equation 41, except with the function $f_{\varepsilon 2}$ and source term S_ε redefined as:

$$f_{\varepsilon 2} = \frac{\tilde{\varepsilon}}{\varepsilon}\left[1 - \left(\frac{C_{\varepsilon 2} - 1.4}{C_{\varepsilon 2}}\right)\exp\left(\frac{\tilde{R}_t}{6}\right)^2\right] \tag{54}$$

$$S_\varepsilon = 0.25\nu\frac{k}{\varepsilon}\overline{u_ju_k}\frac{\partial^2 U_i}{\partial x_j \partial x_l}\frac{\partial^2 U_i}{\partial x_k \partial x_l} \tag{55}$$

A2 Near-wall modelling

The presence of a wall in a particular flow, and specifically the existence of the no-slip condition on the velocity, ensures that viscous effects will always be influential in the region just adjacent to the wall, regardless of how high the Reynolds number of the bulk flow is. Resolving this region places requirements on the near-wall mesh which can quickly become computationally prohibitive in very high Re flows.

The wall function approach aims to remove this requirement by providing an algebraic relationship between variables at the wall and variables at the first computational node adjacent to the wall. This allows (requires) the first node to be placed outside of the viscous sublayer, reducing the computational demand of the mesh. Two wall function approaches have been considered: the standard wall function (SWF) and the newer, more advanced, analytical wall function (AWF).

A.2.1 Standard wall function (SWF)

In the standard wall function, the first near-wall grid node is placed far enough away from the wall to be situated in the fully turbulent region of the near-wall flow. If at the point, the mean velocity U is supposed to be a function only of the distance y from the wall, then the assumption of local equilibrium can be used to formulate an expression for the velocity of the form

$$U^* = \frac{1}{\kappa}\ln(Ey^*) \tag{56}$$

where $\kappa \approx 0.41$ is the von Karman constant, $E \approx 8.4$ and;

$$U^* = \frac{U_P C_\mu^{1/4}\sqrt{k_P}}{\tau_w/\rho} \tag{57}$$

$$y^* = \frac{y_P C_\mu^{1/4}\sqrt{k_P}}{\nu} \tag{58}$$

The subscript P indicates quantities evaluated at the first near-wall node. The wall shear stress can then be computed as

$$\tau_w = \frac{\kappa C_\mu^{1/4}\rho\sqrt{k_P}U_P}{\ln(Ey_P^*)} \tag{59}$$

Other quantities of interest, including cell averaged turbulent quantities, can then be computed. The coefficient C_μ is taken as per Table 3.

A.2.2 Analytical wall function (AWF)

The analytical wall function arose from work conducted at UMIST during the early 2000's (Craft *et al.* 2002, 2004; Gerasimov 2004). In it, the wall shear stress is obtained through the analytical solution of a simplified near-wall version of the wall-parallel mean momentum equation

$$\frac{\partial}{\partial y^*}\left[(\mu+\mu_t)\frac{\partial U}{\partial y^*}\right] = \underbrace{\frac{\nu^2}{k_P}\left[\rho U\frac{\partial U}{\partial x}+\frac{\partial P}{\partial x}\right]}_{C_U} \tag{60}$$

The standard wall function, presented in Appendix A.2.1, may be regarded as resulting from neglecting entirely the effects of convection and pressure gradient on the right hand side of Equation 60.

In order to permit analytical integration of Equation 60, a simple distribution of μ_t over the near-wall cell is prescribed

$$\frac{\mu_t}{\mu} = \begin{cases} 0, & y^* < y_v^* \\ \kappa^*(y^* - y_v^*), & y^* \geq y_v^* \end{cases} \quad 61$$

where $\kappa^* = C_\mu C_l$. The coefficient C_μ is taken as per Table 3, $C_l = 2.55$ and $y_v^* \equiv y_v\sqrt{k_P}/\nu$, where y_v is the edge of the viscous sublayer. If it is further supposed that the convective and wall-parallel pressure gradient terms do not change across the near-wall cell (a standard treatment in the finite volume method), the C_U term on the RHS of Equation 60 can be treated as constant. Equation 60 can then be integrated first across the viscous sublayer $(y^* < y_v^*)$ and then across the fully turbulent region $(y^* \geq y_v^*)$. At the interface, $y^* = y_v^*$, the mean velocity U and its normal gradient are made continuous across the two regions. The resultant velocity profile in the turbulent region and the wall shear stress can then be obtained as:

$$U = \frac{C_U}{\kappa^*}\left[y^* - \left(\frac{1}{\kappa^*} - y_v^*\right)\ln y^*\right] + \frac{A}{\kappa^*}\ln y^* + B \quad 62$$

$$\tau_w = \frac{\sqrt{k_P}}{\nu_v}A \quad 63$$

where

$$A \equiv \frac{\mu_v U_n - \left(\frac{C_U}{\kappa^*}\right)\left[y_n^* - y_v^* - \left(\frac{1}{\kappa^*} - y_v^*\right) + \frac{\kappa^* y_v^*}{2}\right]}{\ln y_n^*} \quad 64$$

$$B \equiv y_v^* C_U\left(\frac{y_v^*}{2} - \frac{1}{\kappa^*}\right) + A y_v^* \quad 65$$

In the definition for A (Equation 64), quantities with subscript n are evaluated at the surface of the control volume most distant from the wall.

DOCUMENT INFORMATION

Project : Project FORTE - Nuclear Thermal Hydraulics Research & Development

Report Title : Assessment of RANS Turbulence Model Performance in Tight Lattice LWR Fuel Subchannels

Client : Department for Business, Energy and Industrial Strategy (BEIS)

Report No. :	FNC 53798/48654R	**Compiled By :**	Dr D. Wilson (The University of Manchester)
Issue No. :	1	**Verified By :**	Prof H. Iacovides (The University of Manchester)
Date :	August 2019	**Approved By :**	C. Howlett

Originating Office: FRAZER-NASH CONSULTANCY LIMITED
The Cube, 1 Lower Lamb Street, Bristol, BS1 5UD
T: +44 (0)117 9226242 F: +44 (0)117 9468924 W: www.fnc.co.uk

Frazer-Nash Consultancy Ltd
The Cube
1 Lower Lamb Street
Bristol
BS1 5UD

T +44 (0)117 9226242
F +44 (0)117 9468924

www.fnc.co.uk

Offices at:
Bristol, Burton-on-Trent, Dorchester,
Dorking, Glasgow, Plymouth, Warrington
and Adelaide